








# Spin-to-charge conversion efficiency in the topological insulator $\text{Bi}_2\text{Te}_3$ and heavy metals W and Pt stacked with the ferromagnetic Weyl semimetal $\text{Co}_2\text{MnGa}$

Nikita Sharma , Nakul Kumar , Lalit Pandey,\*, Nanhe Kumar Gupta ,<sup>†</sup> Soumyarup Hait ,<sup>‡</sup> Shubhashish Pati ,  
Abhay Pandey , and Sujeet Chaudhary <sup>§</sup>

*Thin Film Laboratory, Department of Physics, Indian Institute of Technology Delhi, New Delhi 110016, India*



(Received 5 April 2024; revised 25 July 2024; accepted 14 August 2024; published 4 September 2024)

The Weyl semimetal  $\text{Co}_2\text{MnGa}$  (CMG) has recently attracted significant attention in the field of condensed matter physics because of its unique topological features along with the simultaneous presence of ferromagnetism at room temperature. Utilizing these remarkable properties of CMG for the spintronic applications will be of great interest both from fundamental as well as technological viewpoints. However, the investigation of spin pumping by means of the inverse spin Hall effect (ISHE) is not yet explored in this material. Here, we report the spin generation, spin propagation, and detection of the efficiency of spin-to-charge conversion (SCC) from CMG to different nonmagnetic (NM) layers such as heavy metals like Pt and W and topological materials like  $\text{Bi}_2\text{Te}_3$  through ISHE. The ferromagnetic resonance analyses clearly revealed the dependence of spin relaxation on the spin-orbit coupling strength of the nonmagnets and the concerned interface quality. A large spin mixing conductance of  $\sim 1.8 \times 10^{19} \text{ m}^{-2}$  is observed for W and a quite high value of spin Hall angle of  $\sim 1.5$  is evidenced for  $\text{Bi}_2\text{Te}_3$  in these CMG based heterostructures. Importantly, a correlation is also established between the interfacial spin transport efficiency and the SCC efficiency with the quality of the NM layer as well as the associated interface. The findings obtained are fortified by the longitudinal spin Seebeck effect (LSSE) measurements. The anomalous Nernst contribution is separated from the spin Seebeck contribution by employing measurements in both in-plane magnetized and out-of-plane magnetized configurations. The anomalous Nernst coefficient for a 20-nm polycrystalline CMG film is found to be independent of measurement geometry with a value estimated to be  $0.41 \mu\text{V/K}$ . The results of the LSSE are coherent with the ISHE measurements obtained for different CMG/NM bilayers. This detailed analysis is fundamentally very vital regarding the underlying principles of spin transport and SCC, and is expected to provide key insights for the strategic fabrication and optimization of spintronic devices.

DOI: [10.1103/PhysRevB.110.094402](https://doi.org/10.1103/PhysRevB.110.094402)

## I. INTRODUCTION

Magnetic Weyl semimetals (MWSMs), where time-reversal symmetry breaking induces the splitting of Weyl points, is a host of intriguing magnetotransport phenomena arising due to the interplay between magnetism and Weyl fermionic physics [1,2]. These phenomena encompass the gigantic anomalous Hall effect (AHE) and spin caloritronics such as anomalous Nernst effect (ANE) [2,3]. Among all the known MWSM materials,  $\text{Co}_2\text{MnGa}$ , a full Heusler ferromagnet (FM), stands out as a particularly promising candidate for room temperature applications, with a high Curie temperature ( $T_c \sim 700 \text{ K}$ ) and substantial spin polarization at the Fermi surface [4,5]. Merging these remarkable spin transport characteristics of Heusler alloys with the distinctive band structure

of Weyl semimetals could unveil novel phenomena, offering exciting prospects for spintronics driven by nontrivial topological band physics.

In spintronic device applications, efficient generation, propagation, and detection of spin current are very crucial. Specifically, the spin-to-charge conversion (SCC) or vice versa has garnered special attention due to its huge promise of dissipationless working of spintronic devices. For the fulfillment of this promise, an efficient SCC process between a ferromagnet and a nonmagnet with high spin-orbit coupling (SOC) is a prerequisite [6]. In this regard, ferromagnetic resonance induced generation of spin current in a ferromagnet and spin pumping induced spin current propagation to an adjacent high spin-orbit coupled nonmagnet is a well-known procedure. The efficiency of spin transport across the interface can be understood in terms of effective spin mixing conductance ( $g_{\text{eff}}^{\uparrow\downarrow}$ ) [7]. For the examination of the SCC, the well-known method, namely, the inverse spin Hall effect (ISHE), is generally utilized wherein the conversion of spin pumping induced transversal spin current to charge current is measured. The resulting transverse voltage ( $\vec{V}_{\text{ISHE}}$ ) so produced is related to spin current ( $\vec{J}_s$ ) through the relation [8]

$$\vec{V}_{\text{ISHE}} \propto \theta_{\text{SH}} |\vec{J}_s \times \vec{\sigma}|,$$

\*Present address: Department of Microtechnology and Nanoscience, Chalmers University of Technology, SE-41296 Göteborg, Sweden.

<sup>†</sup>Present address: Centre for Magnetic and Spintronic Materials (CMSM), National Institute for Materials Science (NIMS) 1-2-1 Sengen, Tsukuba, Ibaraki 305-0047, Japan.

<sup>‡</sup>Present address: Department of Materials Science and Engineering, National University of Singapore 639798, Singapore.

<sup>§</sup>Contact author: [sujeetc@physics.iitd.ac.in](mailto:sujeetc@physics.iitd.ac.in)

where  $\theta_{\text{SH}}$  is the spin Hall angle (SHA) defining the conversion efficiency between charge current ( $\vec{J}_C$ ) and spin current ( $\vec{J}_s$ ) and  $\vec{\sigma}$  is the unit vector for the spin-polarization direction. Another technique for the generation and manipulation of spin-polarized current within a ferromagnet by placing it in a thermal gradient is the spin Seebeck effect (SSE) [9]. Detecting this effect involves placing a nonmagnet in proximity to the ferromagnet. Here, the spin current generated in the magnetic layer is transmitted into the adjacent NM layer in the case of a FM/NM heterostructure and is converted into a measurable voltage through the inverse spin Hall effect as discussed earlier [10,11]. It bears mentioning that, in the FM/NM bilayer, the measured SSE voltage also contains the unintentional anomalous Nernst effect contribution [12] which arises due to the metallic nature of the FM and the magnetic proximity effect induced in the NM layer. It is very crucial to disintegrate these two effects for a proper fundamental understanding of these processes as well as to find out the intrinsic efficiency parameters [13].

It is worth stating that the efficient interfacial spin transport and SCC at the FM/NM interface critically depends on the type of interfaces and properties of its associated FM and NM layers on either side. For the NM layer, the SOC strength and conductivity play a major role whereas low damping and high spin polarization, in the case of the FM layer, are the deciding factors in generating a large spin current and high value of  $g_{\text{eff}}^{\uparrow\downarrow}$  [14,15]. In this regard, ferromagnetic Heusler alloys such as  $\text{Co}_2\text{MnGa}$  (CMG) with high spin polarization and a low damping parameter [16] are a proper choice for the FM layer while for the NM layer, the heavy metals such as Pt, W, Ta, etc., are the go-to choice due to their high SOC. However, recently, topological insulators (TIs) such as  $\text{BiSb}$  [17],  $\text{Bi}_2\text{Te}_3$  [18],  $\text{Sb}_2\text{Te}_3$  [19], etc., have also gained attention owing to their unmatched SHA [as high as 425 for  $(\text{Bi}_{0.5}\text{Sb}_{0.5})_2\text{Te}_3$  [20]] due to the presence of spin momentum locked topological surface states. For the ferromagnet, given the similar intrinsic and extrinsic scattering mechanisms influencing AHE and spin Hall effect (SHE), alongside similar scaling trends, CMG emerges as a promising contender for achieving a significant SHA. Additionally, theoretical investigations suggest the potential for robust intrinsic SHE in Weyl semimetals [21,22], a notion substantiated by recent experimental findings indicating a SHA of approximately  $\sim -0.19$  in  $L_{21}$  CMG [23]. In our previous study [24], we have reported low damping of  $\sim 6 \times 10^{-3}$  in 20-nm-thin CMG films, which is much lower than previously reported values on  $B2$  ordered polycrystalline CMG thin films [25]. Although a few reports exist on detailed spin transport and SCC studies on other Heusler alloy-based FM/NM heterostructures in which the NM layers used were either heavy metals and/or topological insulators [6,26], to the best of our knowledge spin mixing conductance and SHA via ISHE have not been studied so far in any heterostructures comprising CMG thin films. Also, the literature lacks reports wherein spin pumping resulting from two completely different spin current generation mechanisms [ferromagnetic resonance (FMR) and SSE] is detected in a single FM/NM heterostructure using ISHE measurements. Bosu *et al.* systematically investigated the transverse SSE in thin films of the half-metallic Heusler compound  $\text{Co}_2\text{MnSi/Pt}$  [27]. Another study by Lopes *et al.* includes the effect of mag-

TABLE I. Details of sample under study.

Sr. No.	Sample details	Sample code
1	Si/SiO <sub>2</sub> /CMG (20 nm)/Al (3 nm) <sup>a</sup>	CMG/Al
2	Si/SiO <sub>2</sub> /CMG (20 nm)/Bi <sub>2</sub> Te <sub>3</sub> (10 nm)	CMG/BT
3	Si/SiO <sub>2</sub> /CMG (20 nm)/W (10 nm)	CMG/W
4	Si/SiO <sub>2</sub> /CMG (20 nm)/Pt (10 nm)	CMG/Pt

<sup>a</sup>Thin layer of Al (thickness 3 nm) serves as a capping layer to protect  $\text{Co}_2\text{MnGa}$  (20 nm) film which is naturally oxidized to  $\text{Al}_2\text{O}_3$ .

netic anisotropy on thermoelectric voltage in a  $\text{Co}_2\text{FeAl/W}$  bilayer structure [28]. To the best of our knowledge, except for these two systems, there are no other studies of the SSE in Heusler ferromagnets so far [29].

In the present study, the fascinating realm of spin pumping dynamics in CMG alloy is explored, with a particular focus on the effects of various nonmagnets on this phenomenon. By systematic investigation, we reveal the interplay among SOC, crystal lattice structure, and interface quality that control spin angular momentum transfer between CMG and NM layers. The ISHE measurement is employed to quantitatively evaluate the SHA and also to demonstrate that the integration of distinct nonmagnets of varying SOC strengths with the CMG layer led to a significant improvement in the spin pumping efficiency. Moreover, an extensive analysis of the effective spin mixing conductance is done, providing insight into the effectiveness of spin transfer mechanisms at the CMG/NM boundaries. To support the conclusions drawn from ISHE measurements, the longitudinal SSE measurement is performed on CMG/NM heterostructures providing experimental validation to the observed spin pumping efficiency enhancement.

## II. MATERIALS AND METHODS

Four different samples (details listed in Table I) were deposited on Si substrates using dc magnetron sputtering employing a vacuum system pumped to a base pressure of  $\sim 5 \times 10^{-8}$  Torr, for the spin current transport and SCC study.

The CMG layer is grown using co-sputtering of Co and MnGa targets and the details of the growth process of CMG can be found elsewhere [24]. After the preparation of the CMG layer at 400 °C, the Pt and W layers were deposited at room temperature and  $\text{Bi}_2\text{Te}_3$  (BT) at 200 °C on the CMG layer. All the NM layers were *in situ* deposited by dc magnetron sputtering. The growth details of  $\text{Bi}_2\text{Te}_3$  can be found in Ref. [30]. The information for the deposition parameters of all the samples is given in the Supplemental Material [31]. The details about the measurements performed and their instrumental setup with measurement parameters are given in the Supplemental Material [31].

## III. RESULTS AND DISCUSSION

### A. Structural analysis

The structural quality of all the films is analyzed with glancing angle x-ray diffraction (GIXRD) patterns (recorded at  $\omega = 1.5^\circ$ ). The x-ray diffraction (XRD) spectra for all the samples are shown in Figs. 1(a)–1(d). The detailed structural

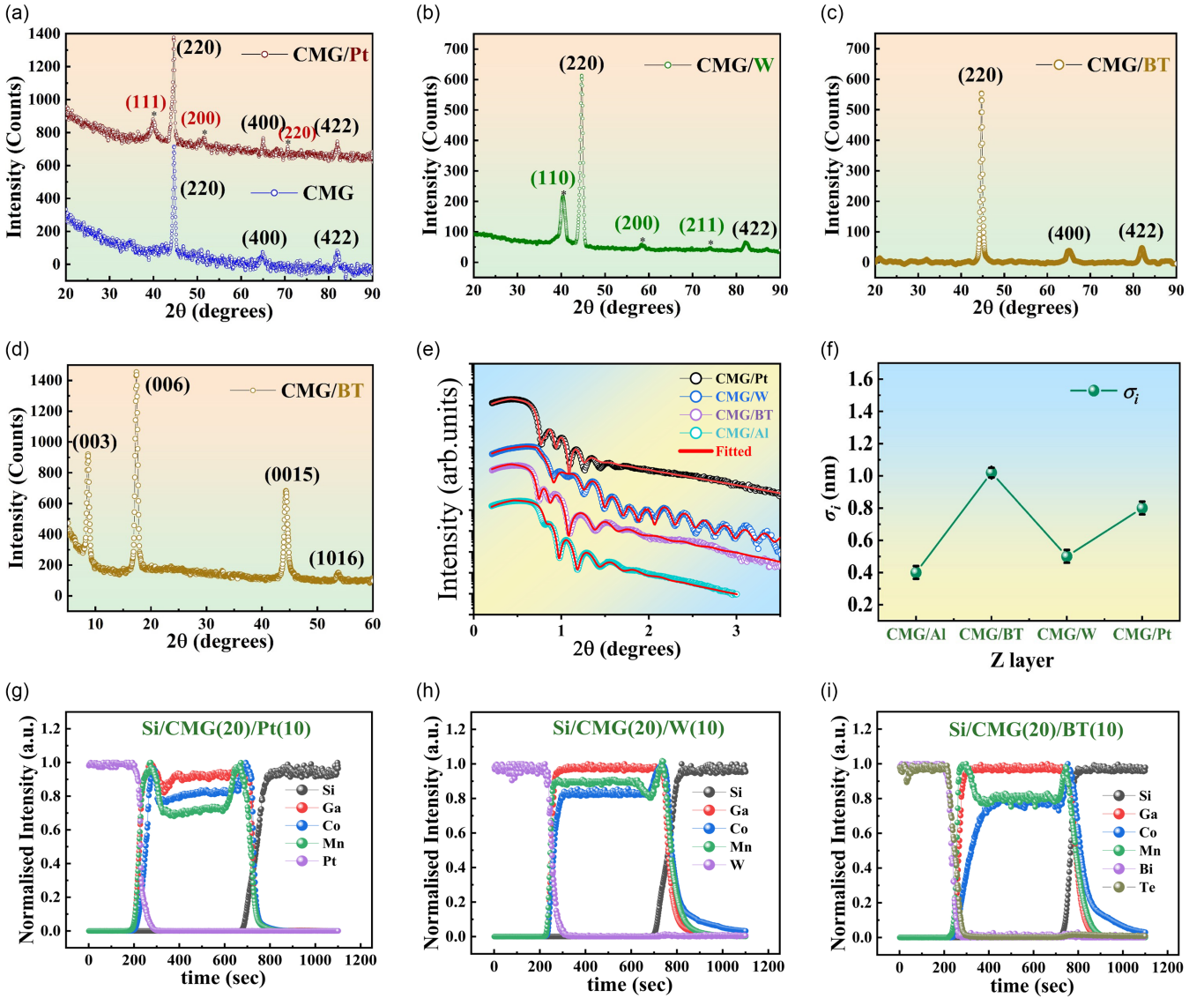


FIG. 1. GIXRD spectra of (a) CMG/Al film (bottom) and CMG/Pt bilayer (top), (b) CMG/W bilayer, and (c) CMG/BT bilayer. (d)  $\theta$ - $2\theta$  Gonio scan of CMG/BT bilayer. (e) XRR profiles of all the samples. (f) Comparison of the interface roughness (obtained from the simulated profiles of XRR data) at the CMG/NM interface for all three bilayer systems together with the surface roughness of the single CMG layer (sample CMG/Al). (g)–(i) present the SIMS depth profiles recorded on three bilayer systems, viz., CMG/Pt, CMG/W, and CMG/BT, respectively.

characterization of the  $B2$  ordered CMG/Al thin film can be found in our previous paper [24]. Safi *et al.* have shown the generation of spin-orbit torque (SOT) from CMG films having different chemical ordering [32]. They have not discerned any apparent advantage in the chemically ordered sample when compared to the disordered counterpart. Remarkably, the disordered  $B2$  phase sample exhibited a higher SOT efficiency in comparison to the fully ordered  $L_{21}$  phase sample. The XRD data of CMG/Pt bilayer [see Fig. 1(a)] shows the polycrystalline growth with Bragg peaks observed at  $2\theta = 40.02^\circ$ ,  $46.41^\circ$ , and  $67.85^\circ$  corresponding to diffractions from (111), (200), and (220) planes of Pt, respectively [33]. The resistivity of the Pt (10 nm) thin film ( $\sim 30 \mu\Omega \text{ cm}$ ) is almost the same as that of the CMG thin film of thickness 20 nm ( $\sim 20 \mu\Omega \text{ cm}$ ). The GIXRD pattern obtained on CMG/W thin film [see Fig. 1(b)] shows the diffraction peaks at

$40.52^\circ$ ,  $58.49^\circ$ , and  $73.25^\circ$  corresponding to the stable alpha ( $\alpha$ ) phase of W. Among the  $5d$  metals, the  $\beta$ -W is reported to have appreciable SCC owing to its superior SHA. However, its high resistance renders it unsuitable for device applications [34,35]. Conversely, the low resistive phase, i.e.,  $\alpha$ -W, has a smaller SHA but exhibits high spin Hall conductivity (SHC) [36]. The larger SHC implies lower energy requirements for generating the same amount of spin current, making it more favorable for device applications [37]. The phase is reconfirmed by the electrical measurement of resistivity of a single layer of W (10 nm) using linear four-probe geometry. The low resistivity of  $58 \mu\Omega \text{ cm}$  measured on it matches with the reported values of  $\alpha$ -W [36]. Figure 1(c) shows the polycrystalline growth of CMG with no peaks corresponding to  $\text{Bi}_2\text{Te}_3$  in a GIXRD scan on CMG/BT bilayer. The  $\theta$ - $2\theta$  Gonio XRD scan

[see Fig. 1(d)] done on CMG/BT bilayer shows that the BT thin film has a preferred orientation with  $2\theta$  values of  $8.23^\circ$ ,  $17.54^\circ$ ,  $44.33^\circ$ , and  $53.62^\circ$  belonging to the  $(0\ 0\ 3n)$  family of planes of the  $\text{Bi}_2\text{Te}_3$  phase [38]. The electrical measurement on a single layer of BT reveals a very high resistivity of  $110\ \mu\Omega\ \text{cm}$ , which is almost five times higher than that of the CMG thin film. The grown BT film is expected to show topological behavior as discussed in detail in our previous paper [30]. The magnetotransport measurement is performed in an out-of-plane magnetic field configuration at different temperatures lying in the range of 3–8 K on single layer BT film. The data is fitted using a Hikami-Larkin-Nagaoka equation and various parameters such as phase coherence length ( $l_\varphi$ ) and the Berry curvature-dependent prefactor ( $\alpha$ ) are estimated to identify the presence of topological phases in this film. The details and discussion of the magnetotransport measurement are given in Supplemental Material Sec. S3 [31].

The x-ray reflectivity (XRR) spectra are recorded on CMG thin film and its heterostructures to infer the quality of the interface between them which is crucial for spintronics-based device applications. The recorded spectra as shown in Fig. 1(e) are fitted with x-ray reflectivity software considering the Si/SiO<sub>2</sub>/CMG/Z/oxide layer stack (where  $Z = \text{BT}, \text{W}, \text{Pt}$ ). The fitted values of density, thickness, and interface/surface roughness of the stacks are listed in Table S2 in the Supplemental Material [31]. The density of each layer either matches the bulk value or is slightly lower than that, and the simulated thickness values mimic the nominal values. The single layer CMG is capped with Al, which is naturally oxidized to Al<sub>2</sub>O<sub>3</sub>. As depicted in Fig 1(f), the interface roughness is slightly higher for the CMG/BT interface compared to the other two heterostructures, which may be due to the growth of BT at 200 °C. The growth rate of the nonmagnets in all three heterostructures is optimized in such a way to achieve a good-quality interface in terms of low roughness. The presence of clear Kiessig fringes observed over the whole measurement range of  $2\theta (= 6^\circ)$  suggests the good interface quality in the case of CMG/W bilayer. The interface quality of the concerned heterostructures has a direct impact on the dynamic properties as can be seen in the ferromagnetic resonance section later.

The interface quality/intermixing is again confirmed by performing secondary ion mass spectroscopy (SIMS) measurements on grown heterostructures. As shown in Figs. 1(g) and 1(h), the depth profiles recorded at RT show a clear transition at the CMG and NM interface, and no evidence of interdiffusion of film elements in the substrate is seen in CMG/W and CMG/Pt bilayers. Though, the slight interdiffusion of cobalt in substrate and nonuniformity in cobalt at the trailing edge close to the Co<sub>2</sub>MnGa/Bi<sub>2</sub>Te<sub>3</sub> interface in the case of CMG/BT bilayer is present [see Fig. 1(i)]. Furthermore, the flat elemental profile of all the elements in both CMG and the NM layers indicates the composition uniformity over the film thickness in all the heterostructures.

It is worth highlighting that in this CMG/BT bilayer, the BT grown over CMG is held by weak van der Waal forces. Therefore, the interface between CMG and BT is sensitive to post annealing conditions. It should also be noted that reversing the stacking sequence in the heterostructure from Si//CMG/BT to Si//BT/CMG would not give the same re-

sults because in the latter case, the growth and annealing of CMG at the optimized 400 °C temperature on already grown BT (whose optimized growth temperature is 250 °C) will significantly affect the bulk SOC and also the topological properties via the surface roughness (due to interdiffusion) of the BT. In fact, the FMR linewidth is increased by a large factor thereby indicating the presence of large inhomogeneity resulting from the inferior interface quality relative to Si//CMG/BT heterostructures, as confirmed from the analysis of the SIMS profiles recorded on the Si//CMG/BT and Si//BT/CMG heterostructures. The latter clearly exhibited evidence of intermixing at the interface of BT and CMG. (See Supplemental Material [31] for the FMR response and SIMS data together with their analyses for these two types of CMG/BT heterostructures).

## B. Dynamic magnetization response using ferromagnetic resonance

The flow and relaxation of spin angular momentum in a FM/NM heterostructure can be investigated from the in-plane FMR measurements. In our microstrip-based FMR setup, an in-plane external magnetic field ( $H_{\text{ext}}$ ) is swept at a constant microwave frequency ( $f$ ) over the frequency range of 5–11 GHz to obtain the resonance condition of the film [39]. The obtained FMR spectra of all the samples at different frequency  $f$  are fitted using a derivative of the Lorentzian function, which consists of symmetric and antisymmetric components to obtain the values of resonance field ( $H_r$ ) and linewidth ( $\Delta H$ ) [40].

$$\frac{d\chi}{dH} = -S \frac{\left(\frac{\Delta H}{2}\right)^2 (H_{\text{ext}} - H_r)}{\left[\left(\frac{\Delta H}{2}\right)^2 + (H_{\text{ext}} - H_r)^2\right]^2} + A \frac{\left(\frac{\Delta H}{2}\right) \left[\left(\frac{\Delta H}{2}\right)^2 - (H_{\text{ext}} - H_r)^2\right]}{\left[\left(\frac{\Delta H}{2}\right)^2 + (H_{\text{ext}} - H_r)^2\right]^2}. \quad (1)$$

In Eq. (1),  $S$  and  $A$  are the symmetric and antisymmetric absorption coefficients, respectively. Now, the plots of resonance frequency ( $f$ ) versus  $H_r$  and  $\Delta H$  versus  $f$ , shown in Figs. 2(a) and 2(b) are fitted using linewidth Eq. (2) [41] and Kittel's Eq. (3) [42] to evaluate the effective damping constant ( $\alpha_{\text{eff}}$ ), inhomogeneous linewidth ( $\mu_0\Delta H_0$ ), effective magnetization ( $\mu_0 M_{\text{eff}}$ ), and effective in-plane anisotropy field ( $\mu_0 H_K$ ). The values obtained for all the parameters and the roughness value at the CMG/NM interface ( $\sigma_{\text{CMG/NM}}$ ) for different samples under consideration are presented in Table II.

$$\mu_0\Delta H = \mu_0\Delta H_0 + \frac{4\pi\alpha_{\text{eff}}}{\gamma} f, \quad (2)$$

$$f = \frac{\mu_0\gamma}{2\pi} [(H_r + H_K)(H_r + H_K + M_{\text{eff}})]^{1/2}. \quad (3)$$

The value of  $\mu_0 H_K$  is quite low for CMG/Al indicating the weak anisotropy present in the CMG film. The same has been confirmed with the magneto-optical Kerr effect (MOKE) data as presented in the Supplemental Material [31] depicting the isotropic nature of the CMG thin film. As interpreted from Fig. 2(d), the introduction of the NM on CMG has slightly enhanced the anisotropy in the case of CMG/Pt bilayer as clearly seen with the increase in the value of  $\mu_0 H_K$  with not

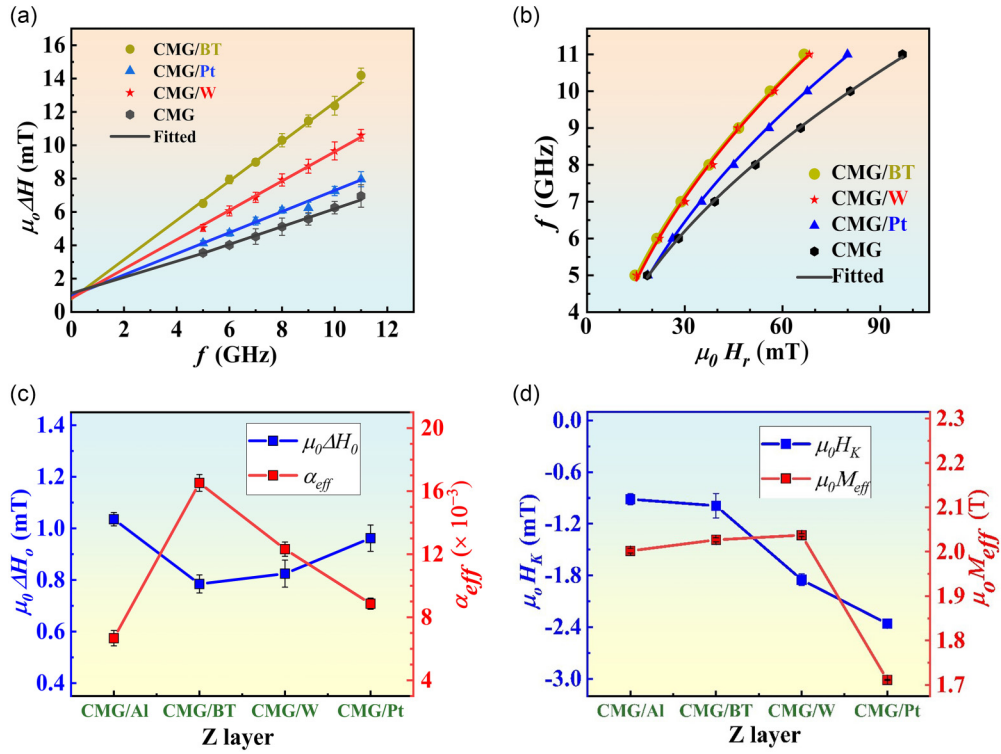


FIG. 2. (a)  $\mu_0\Delta H$  vs  $f$  and (b)  $f$  vs  $\mu_0 H_r$  curves for all four systems under investigation. While the symbols represent the experimental data, the solid lines are fit to the data using Eqs. (1) and (2), respectively. Variation in (c)  $\mu_0\Delta H_0$  (left) and  $\alpha_{\text{eff}}$  (right) and (d)  $\mu_0 H_K$  (left) and  $\mu_0 M_{\text{eff}}$  (right) as a function of different bilayer systems.

much change observed in the case of CMG/BT. The same trend could be seen in the values of effective magnetization in Fig. 2(d). The reason for low effective in-plane magnetization for CMG/Pt bilayer could be the induced out-of-plane anisotropy in CMG due to the magnetic proximity effect (MPE) in Pt. There are many reports claiming the presence of MPE when a Pt film (at thicknesses comparable to and less than the spin diffusion length) is deposited on a thick FM metal [43–45].

In Eq. (2), the  $\mu_0\Delta H_0$  is the inhomogeneous broadening of the linewidth due to extrinsic factors such as scattering from magnetic inhomogeneities. In Fig. 2(c), the variation of  $\mu_0\Delta H_0$  and  $\alpha_{\text{eff}}$  is plotted with different NM materials. The low value of  $\mu_0\Delta H_0$  for bare CMG and its bilayers with nonmagnets indicates the good quality of the interface. A large spin pumping is observed in the CMG/BT heterostructure with an enhancement of  $\sim 175\%$  ( $\alpha_{\text{eff}}$  increased from  $6.67 \times 10^{-3}$  to  $16.52 \times 10^{-3}$ ). Such a large enhancement in  $\alpha_{\text{eff}}$  with TIs as a high SOC material is reported in the literature [19,46]. The CMG/W(Pt) bilayers show an increment

in  $\alpha_{\text{eff}}$  from  $6.67 \times 10^{-3}$  to  $12.32$  ( $8.86$ )  $\times 10^{-3}$  with an enhancement of 82.5% (31.2%). There are numerous additional influences, including interface effect, impurities, and MPEs, which have the potential to augment the  $\alpha_{\text{eff}}$  value of the system. To investigate the MPE at the interface, the out-of-plane (OOP) magnetization hysteresis (MH) loops for three bilayer system and reference sample CMG/AI are obtained (the data and its analysis are presented in the Supplemental Material [31]). The OOP-MH loop in all three samples marks the presence of proximity effect. Nonetheless, it has been reported in FM/BT bilayer that the ferromagnetism induced by the magnetic proximity effect via van der Waal bonding in  $\text{Bi}_2\text{Te}_3$  is too weak [47].

The crucial aspect lies in the variation of  $\alpha_{\text{eff}}$  with the nonmagnet. Within a single FM layer (or capped with a material with low SOC strength, e.g., Al in the present case),  $\alpha_{\text{eff}}$  essentially signifies the relaxation of spin angular momentum within the crystal lattice through scattering mechanisms within the FM layer. However, when a NM layer characterized by high SOC strength, is placed adjacent to the FM layer,

TABLE II. Different parameters obtained by fitting the experimental data using Eqs. (2) and (3).

Sample code	$\alpha_{\text{eff}}$ ( $\times 10^{-3}$ )	$\mu_0 M_{\text{eff}}$ (T)	$\mu_0 H_K$ (mT)	$\mu_0\Delta H_0$ (mT)	$\sigma_{\text{CMG/NM}}$ (nm)
CMG/Al	$6.671 \pm 0.486$	$2.001 \pm 0.005$	$-0.914 \pm 0.061$	$1.045 \pm 0.026$	$0.4 \pm 0.04$
CMG/BT	$16.520 \pm 0.531$	$2.026 \pm 0.004$	$-0.990 \pm 0.142$	$0.784 \pm 0.035$	$1.02 \pm 0.03$
CMG/W	$12.325 \pm 0.452$	$2.037 \pm 0.003$	$-1.853 \pm 0.066$	$0.824 \pm 0.052$	$0.5 \pm 0.04$
CMG/Pt	$8.866 \pm 0.355$	$1.711 \pm 0.001$	$-2.362 \pm 0.037$	$0.962 \pm 0.051$	$0.8 \pm 0.01$

the spin angular momentum does not solely relax within the FM lattice; rather, it also tends to transfer into the adjoining NM layer, a phenomenon known as spin pumping [48]. Consequently, an augmentation in  $\alpha_{\text{eff}}$  becomes evident. This transfer of spin angular momentum is highly dependent on the quality of the interface between the nonmagnet/ferromagnet and the strength of SOC in the NM layer [14,15]. There are further crucial parameters associated with spin pumping that must also be calculated, such as spin mixing conductance and effective spin current density in the NM layer, to effectively quantify the spin pumping effect.

To calculate the intrinsic spin mixing conductance and spin diffusion length, three NM thickness-dependent series are also made by varying the NM layer thickness ( $t_{\text{NM}} = 5, 7, 10, 15,$  and  $20$  nm). The values of  $\alpha_{\text{eff}}$  obtained at different thickness of the NM layer is given in the Supplemental Material [31]. The variation of  $\alpha_{\text{eff}}$  as a function of  $t_{\text{NM}}$  is fitted using Eq. (4) [49,50].

$$\alpha_{\text{eff}} - \alpha_{\text{CMG}} = g^{\uparrow\downarrow} \frac{g\mu_B}{4\pi M_S t_{\text{CMG}}} (1 - e^{-2t_{\text{NM}}/\lambda_d}). \quad (4)$$

From the fitted equation, we have obtained the value of intrinsic spin mixing conductance ( $g^{\uparrow\downarrow}$ ) at the CMG/NM interface and spin diffusion length ( $\lambda_d$ ) of the nonmagnet ( $Z = \text{BT}, \text{W}, \text{Pt}$ ). The value of  $g^{\uparrow\downarrow}$  ( $\lambda_d$ ) for BT, W, and Pt are found to be  $9.59 \pm 0.35 \times 10^{19} \text{ m}^{-2}$  ( $14.61 \pm 0.23$  nm),  $5.76 \pm 0.52 \times 10^{19} \text{ m}^{-2}$  ( $2.32 \pm 0.10$  nm), and  $2.61 \pm 0.51 \times 10^{19} \text{ m}^{-2}$  ( $7.68 \pm 0.17$  nm), respectively.

The value of spin diffusion length ( $\lambda_d$ ) of W and Pt matches the reported values [51,52] whereas for BT, it is at the upper end of the reported values [45]. The high value of  $\lambda_d$  can be attributed to the low resistivity of our BT thin films as the  $\lambda_d$  is inversely proportional to the resistivity of the material [51,53]. Also, the  $\lambda_d$  of a material depends upon the crystal quality, measurement temperature, and relative strength of the surface vs bulk contributions in the sample. The long spin diffusion length in this work indicates the higher bulk to surface contribution of SOC in BT thin film. The highest and lowest  $g^{\uparrow\downarrow}$  among three heavy metals is reported for the CMG/BT and CMG/Pt bilayer system, respectively. For CMG/BT and CMG/W, the value of  $g^{\uparrow\downarrow}$  is slightly higher than the reported values in the literature [54,55] whereas for CMG/Pt, it matches with the reported values [6,7,26]. Since the interface roughness is highest in CMG/BT bilayer (refer to Table II), it is already expected to obtain the overestimated  $g^{\uparrow\downarrow}$ . The variation in  $g^{\uparrow\downarrow}$  value is majorly affected by (1) spin memory loss at the interface (arising from interface disorder or alloying) and (2) spin backflow at the CMG and NM interface [56]. The thickness is kept same for all the three nonmagnets but their resistivity and also  $\lambda_d$  could be different. However, it should be noted here that Eq. (4), from which  $g^{\uparrow\downarrow}$  is computed, does not consider the spin backflow from any of the CMG interfaces [49] and is independent of the nature of the NM layer. Hence, we have also calculated the  $g_{\text{eff}}^{\uparrow\downarrow}$  [using Eq. (5)] which includes the effective spin accumulation at the interface and which thereby accounts for spin backflow, if any,

according to which  $g_{\text{eff}}^{\uparrow\downarrow}$  is given by [54]

$$g_{\text{eff}}^{\uparrow\downarrow} = \frac{g^{\uparrow\downarrow}}{1 + \frac{g^{\uparrow\downarrow}}{g_{\text{ext}}}}, \quad (5)$$

where  $g_{\text{ext}} = \frac{h}{e^2 \rho_{\text{NM}} \lambda_d} \tanh(\frac{t_{\text{NM}}}{\lambda_d})$  is a material-dependent parameter having units of conductance and  $\rho_{\text{NM}}$  is the resistivity of the NM layer. The value of  $g_{\text{eff}}^{\uparrow\downarrow}$  computed for different nonmagnets is tabulated below in Table III. The value of  $g_{\text{eff}}^{\uparrow\downarrow}$  for CMG/BT, as compared to CMG/W and CMG/Pt, is found to be reduced by a substantial amount owing to its (1) high resistivity and (2)  $\lambda_d > t_{\text{NM}}$ . The value of  $g_{\text{eff}}^{\uparrow\downarrow}$  for CMG/W is highest and quite higher than those reported in the literature for  $\alpha$ -W [57–59]. This implies a large spin generation in CMG due to its high intrinsic SOT efficiency, and also a good-quality interface between CMG and W that has led to very efficient spin injection. Understandably, such a large value of spin mixing conductance will yield a large spin current in an adjacent nonmagnetic layer.

The enhancement in damping is interpreted in terms of the generation of spin current in NM layers by a pumping mechanism at the bilayer interface. The effective spin current density is calculated by the relation [60]

$$|\vec{J}_s| \approx \left( \frac{g_{\text{eff}}^{\uparrow\downarrow} \hbar}{8\pi} \right) \left( \frac{\mu_0 h_{\text{rf}} \gamma}{\alpha_{\text{eff}}} \right)^2 \times \left[ \frac{\mu_0 M_S \gamma + \sqrt{(\mu_0 M_S \gamma)^2 + (4\pi f)^2}}{(\mu_0 M_S \gamma)^2 + (4\pi f)^2} \right] \left( \frac{2e}{\hbar} \right), \quad (6)$$

where  $h_{\text{rf}}$  is the rf field (22 mOe) in the microstrip of our waveguide. The estimated values of  $J_s$  and  $g_{\text{eff}}^{\uparrow\downarrow}$  for different nonmagnets are shown in Fig. 4(a). The values of  $g_{\text{eff}}^{\uparrow\downarrow}$ ,  $J_s$ , and  $\theta_{\text{SH}}$  for different nonmagnet obtained in the present study are presented in Table III alongside those reported in the literature. The current density  $J_s$  is relatively low for CMG/BT. Generally, the typical TIs are observed to have spin current density lower by an order of magnitude than those of heavy metals [61]. But due to their low current conduction capability, the spin Hall angle is large ( $\sim 1.0$  as reported for  $\text{Bi}_2\text{Te}_3$  [18]). The saturation magnetization values are taken from the experimental data shown in the Supplemental Material [31].

### C. Inverse spin Hall effect measurements

In the preceding section, we discussed the spin current that was generated in CMG and got relaxed at the nonmagnet through spin backflow effect and spin current into the NM layer. However, when spin current enters the nonmagnet with high SOC strength, then due to ISHE, this spin current gets converted into some transverse charge current that can be calculated from the measured ISHE voltage and the dc resistivity of the NM layer. This method of inferring the spin current is very popular and generally used to estimate the SCC, whose efficiency is quantified by spin Hall angle ( $\theta_{\text{SH}}$ ) which can be estimated from the ISHE measurements. We have performed the ISHE measurements on all the bilayer samples using our home-built ISHE setup as shown in the schematic presented in Fig. 3(a). The samples under study are placed at same position with respect to the microstrip fixture to minimize

TABLE III. Effective spin mixing conductance ( $g_{\text{eff}}^{\uparrow\downarrow}$ ), effective spin current density ( $\vec{J}_s$ ), and spin Hall angle ( $\theta_{\text{SH}}$ ) obtained from fitting of Eqs. (5), (6), and (8).

Sample	$g_{\text{eff}}^{\uparrow\downarrow} \times 10^{19} \text{ (m}^{-2}\text{)}$	$J_s \times 10^6 \text{ (A m}^{-2}\text{)}$	$\theta_{\text{SH}}$	Reference
$\text{Co}_2\text{MnGa/Bi}_2\text{Te}_3$	$1.243 \pm 0.140$	$0.010 \pm 0.023$	$1.4774 \pm 0.0081$	This work
$\text{Co}_2\text{MnGa/W}$	$1.806 \pm 0.214$	$0.267 \pm 0.035$	$-0.0836 \pm 0.0009$	
$\text{Co}_2\text{MnGa/Pt}$	$0.795 \pm 0.109$	$0.122 \pm 0.003$	$0.0998 \pm 0.0011$	
$\text{Bi}_2\text{Sb}_3/\text{CoFeB}$	1.2	2.8	0.34	[46]
$\text{Bi}_2\text{Te}_3/\text{NiFe}$			1.00	[18]
$\text{Bi}_2\text{Te}_3/\text{Ti/CoFeB}$			0.08	[62]
$\text{Bi}_2\text{Se}_3/\text{CoFeB}$	0.6	4.1		[63]
$\text{Bi}_2\text{Se}_3/\text{CoFeB}$	6.5	10.0	0.33	[46]
$\text{Bi}_2\text{Se}_3/\text{CoFeB}$			16.80	[64]
$\text{Bi}_2\text{Se}_3/\text{NiFe}$			2.50–3.00	[65]
$\text{NiFe/Pt}$	1.5		0.19	[7]
$\text{CoFeB/Pt}$	3.9	2.9	0.09	[66]
$\text{Co}_2\text{MnSi/Pt}$	1.5		0.04	[26]
$\text{Co}_2\text{Fe}_{0.4}\text{Mn}_{0.6}\text{Si/Pt}$	4.0		0.02	[60]
$\alpha\text{-W/CoFeB}$			-0.06	[67]
$\alpha\text{-W/CoFeB}$			-0.07	[35]

any error due to position dependence of the power of the microwave signal absorbed in the sample. The measurements are carried out at 5 GHz frequency at the maximum output power (5 dBm) available from the vector network analyzer

(model 8719ES from M/S HP Inc.). Even at such a relatively low power, a reasonably good strength of ISHE voltage signal (approximately microvolts) could be observed for all the samples. In Figs. 3(b)–3(d), the measured ISHE voltage ( $V_{\text{meas}}$ ) of

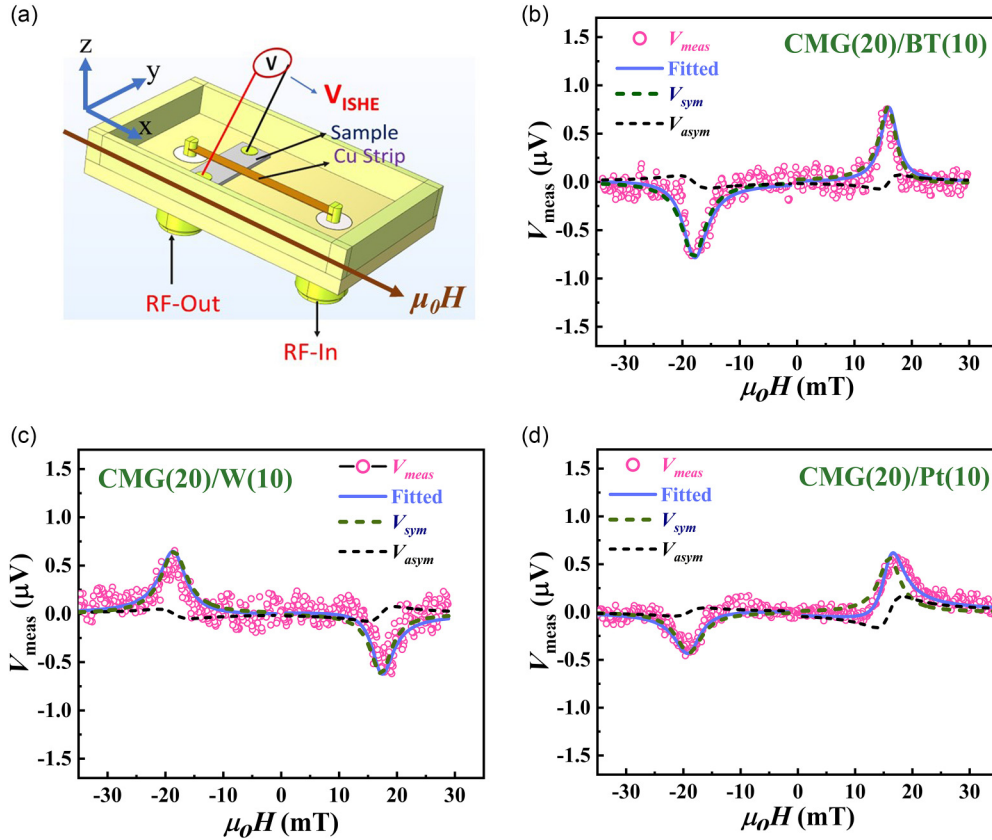


FIG. 3. (a) Schematic of the setup used for ISHE measurements. (b) ISHE voltage ( $V_{\text{meas}}$ ) measured across the sample as a function of the strength of the dc magnetic field ( $\mu_0 H$ ) applied along the microstrip [see (b)] for CMG/BT, (c) CMG/W, and (d) CMG/Pt. Open symbols show the experimental data. Solid lines are the fits to the experimental data using Eq. (7). Blue and black dashed lines show the symmetric ( $V_{\text{sym}}$ ) and antisymmetric ( $V_{\text{asym}}$ ) components of the ISHE voltage, respectively.

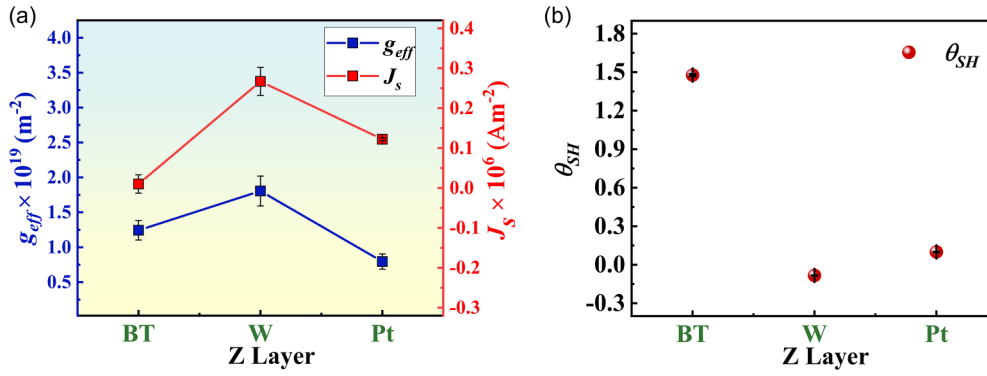


FIG. 4. (a) Effective spin mixing conductance ( $g_{\text{eff}}^{\uparrow\downarrow}$ ) (left) and effective spin current density ( $J_s$ ) (right) as a function of different nonmagnets. (b) Spin Hall angle ( $\theta_{\text{SH}}$ ) as a function of different nonmagnets.

the CMG/NM heterostructures is plotted as a function of the applied magnetic field strength ( $\mu_0 H$ ) for different bilayers where field is swept in the positive  $x$  direction.

It is worth noting that the contribution in the measured ISHE voltage may jointly originate from spin pumping as well as due to different spin rectification effects (SREs) such as AHE, anisotropic magnetoresistance (AMR), etc. [68]. However, it is quite well known that if the sign of  $V_{\text{meas}}$  gets reversed as the applied field reverses, the contribution in  $V_{\text{meas}}$  is primarily from spin pumping rather than different rectification effects [60]. The line shape analysis of this data gives actual quantitative information of these two contributions from the measured voltage in these bilayer systems. Therefore, the  $V_{\text{meas}}$  versus  $H$  plots are fitted with Lorentzian equation (7) [69], which is given by

$$V_{\text{meas}} = V_{\text{sym}} \frac{(\Delta H)^2}{(H - H_r)^2 + (\Delta H)^2} + V_{\text{asym}} \frac{2\Delta H(H - H_r)}{(H - H_r)^2 + (\Delta H)^2}, \quad (7)$$

where  $V_{\text{sym}}$  and  $V_{\text{asym}}$  are the symmetric and antisymmetric coefficients, respectively. Solid lines are the fits to the experimental data. The  $V_{\text{sym}}$  (blue dashed lines) and  $V_{\text{asym}}$  (black dashed lines) are fitted separately in Figs. 3(b)–3(d). The  $V_{\text{sym}}$  contains a major contribution from spin pumping effects such as the ISHE. On the other hand, the  $V_{\text{asym}}$  component accounts for the SRE contributions due to AMR and AHE [68]. It can be observed from the fitting that the symmetric part majorly contributes in the  $V_{\text{meas}}$  indicating the dominance of spin pumping as compared to other rectification effects. As can be seen from Figs. 3(b)–3(d), in the present case, the strength of the ISHE voltage signal obtained in three systems is consistent with the fact that the ISHE voltage is inversely proportional to the conductivity of the NM layer [26].

The positive value of  $V_{\text{sym}}$  for BT and Pt and the negative value for W at positive field  $H$  indicates the positive and negative spin Hall angle of these nonmagnets, respectively, which is consistent with the literature. The value of  $\theta_{\text{SH}}$  is calculated for BT, W, and Pt by using the following expression [14,60]:

$$V_{\text{ISHE}} = \left( \frac{w_y}{\sigma_{\text{FM}} t_{\text{FM}} + \sigma_{\text{Pt}} t_{\text{Pt}}} \right) \times \theta_{\text{SH}} \lambda_{\text{Pt}} \tanh\left(\frac{t_{\text{Pt}}}{2\lambda_{\text{Pt}}}\right) |\vec{J}_s|. \quad (8)$$

The resistivities ( $\rho$ ) of the CMG and NM layers, measured using the four-probe technique, are mentioned in the structural characterization section. The corresponding values of conductivity ( $\sigma$ ) of the individual layers are calculated. The rf field ( $h_{\text{rf}}$ ) and the CPW microstrip width ( $w_y$ ) for our setup is taken as 22 mOe and 1.5 mm, respectively. The obtained values of  $\theta_{\text{SH}}$  are plotted for the three nonmagnets in Fig. 4(b). In this study, the value of  $0.0998 \pm 0.0011$  of the SHA for Pt matches the literature values [66]. The  $\theta_{\text{SH}}$  value of  $-0.0836 \pm 0.0009$  is obtained for  $\alpha$ -W, which is higher than the reported values [35,67], possibly due to its low resistance and good-quality interface. Despite significant spin backflow owing to high interface roughness, BT exhibits the highest  $\theta_{\text{SH}}$  value of  $1.4774 \pm 0.0081$ , which is attributed to its strong spin-orbit coupling and topological nature. The large SHA obtained in this FM/TI system makes BT a suitable candidate alongside CMG for SCC-based applications. The values of SHA correlate with the strength of the SOC in different NM materials under study, i.e., highest for BT and lowest for  $\alpha$ -W [24].

#### D. Spin Seebeck effect measurement

In the previous section, the detection of spin current is explored, and SCC efficiency is estimated through ISHE measurements by utilizing the spin pumping phenomena. Another way to do this is to generate the spin current by creating a temperature gradient in the structure. This is called the SSE phenomena [27]. To have a more comprehensive understanding of the SCC in these bilayer systems, we have done thermospin measurements with a temperature gradient of 15 K in the longitudinal geometry as shown in Fig. 5(a). The longitudinal geometry (in which a temperature gradient is applied across the two surfaces of the film, i.e., across the film thickness) is advantageous due to the absence of anomalies stemming from thermal shunting of the temperature gradient from the two adjacent top and bottom layers and/or the underlying substrate, wherein a significant mismatch could exist between the thermal conductivity of the magnetic thin film and the adjacent layers and/or the substrate [70].

The schematic depicting the magnetization rotation angle  $\alpha$  along with measurement geometry is shown in Fig. 5(a). Figure 5(c) showing that the thermospin voltage ( $V_{\text{th}}$ ) (measured with a field  $H = 100$  mT and temperature gradient



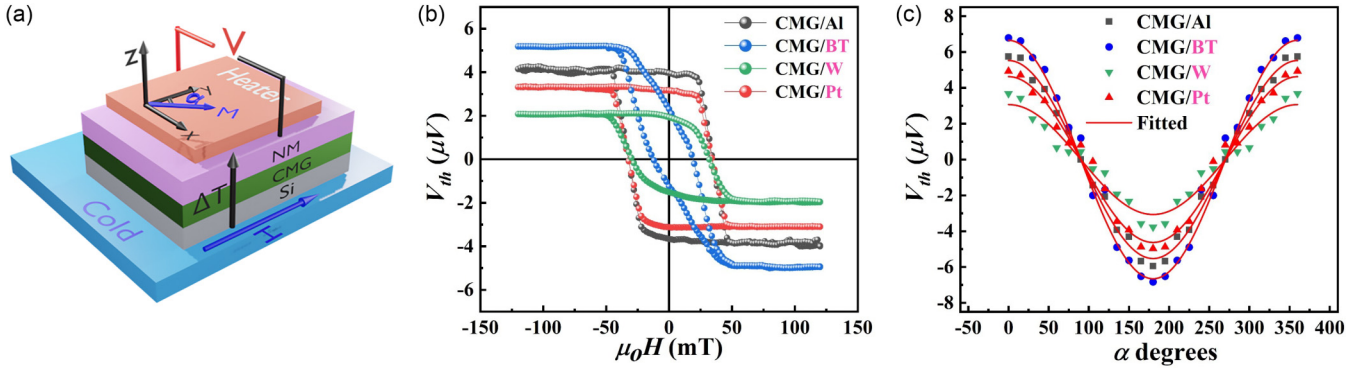


FIG. 5. (a) Schematic showing the magnetization rotation angle  $\alpha$ ;  $x - y$  is the sample plane and the temperature gradient is applied along the  $z$  direction. (b) Thermospin voltage (spin Seebeck+anomalous Nernst voltage) vs applied magnetic field as observed for the different heterostructures. (c) Variation of thermospin voltage with the magnetic field angle  $\alpha$  with applied field  $H = 100$  mT and  $\Delta T = 15$  K. Solid red curve represents the fit with  $A \cos \alpha$ .

$\Delta T = 15$  K) has the field angle dependence given by  $V_{th} \propto \cos \alpha$ . The data presenting the variation in the thermospin voltage ( $V_{th}$ ) as a function of the applied magnetic field for all the CMG/NM bilayer structures is shown in Fig. 5(b). It needs to be highlighted that the shape of the hysteresis loop obtained in these measurements closely resembles the magnetic hysteresis loop shape (around  $H = 0$ ) observed in the OOP-MH loop (data shown in the Supplemental Material [31]). The asymmetric behavior of  $V_{th}$  with magnetic field exists possibly because of the two different contributions to the measured voltage, i.e., SSE contribution ( $V_{SSE}$ ) and the ANE contribution ( $V_{ANE}$ ) in the CMG layer [70]. The ANE mechanism involves the transfer of spin angular momenta by thermally generated magnons to the itinerant electrons of the ferromagnet mediated by electron-magnon scattering. These itinerant electrons of the ferromagnet get spin polarized and contribute to ANE. Whereas in case of longitudinal SSE (LSSE), as a result of spatial gradient, these thermally generated magnons accumulate near FM/NM interface and pump spin current in the NM layer [29]. It should be emphasized that the CMG itself is reported to show large ANE (2–3  $\mu\text{V}/\text{K}$ ) in an in-plane magnetized (IPM) geometry [when  $H$  is applied parallel ( $\parallel$ ) to the CMG/NM interface and  $\vec{\nabla}T \perp$  CMG/NM interface [see Fig. 6(b)]] due to its Weyl nature [71]. However, the presence of a large ANE does not guarantee the large SSE. Therefore, it is technologically advantageous for the spin caloritronic applications to explore a FM system that shows both large ANE and SSE in different magnetic configurations [29]. The longitudinal configuration is simplest in which a polycrystalline ferromagnet can be used and regarded as a prototype from an application point of view [70]. The electric field generated due to the ANE in metallic ferromagnets, in the presence of temperature gradient  $\vec{\nabla}T$  and magnetization  $\vec{M}$  is governed by the following equation:

$$\vec{E}_{ANE} \propto S_{ANE}(\mu_0 \vec{M} \times \vec{\nabla}T), \quad (9)$$

where  $S_{ANE}$  is the anomalous Nernst coefficient. Thus, the data in Fig. 5(b) also contains the  $V_{ANE}$  vs  $H$  contribution expected from the single layer CMG, which must be suitably corrected.

From Fig. 5(b), the ANE voltage ( $V_{ANE}$ ) for a 20-nm-thick isolated CMG layer is found to be 3.98  $\mu\text{V}$ . The anomalous Nernst coefficient in an IPM configuration can be estimated as  $S_{ANE} = \frac{V_{ANE} t_{CMG}}{L_y \Delta T_{CMG}}$ , where  $L_y$  is the separation between the voltage contacts and  $\Delta T_{CMG}$  is the temperature gradient across the CMG layer.  $\Delta T_{CMG}$  can be extracted from the experimentally measured temperature difference  $\Delta T$  through  $\Delta T_{CMG} \approx (\frac{t_{CMG} \kappa_{substrate}}{t_{substrate} \kappa_{CMG}}) \Delta T$ , where  $t_{substrate}$  is the thickness of the substrate, i.e., Si,  $\kappa_{substrate}$ , and  $\kappa_{CMG}$  are the thermal conductivities of the Si substrate and CMG layer, respectively [72]. Considering  $t_{CMG} = 20$  nm,  $t_{substrate} = 0.5$  mm,  $\kappa_{substrate} = 1.3$  W  $\text{m}^{-1}$   $\text{K}^{-1}$ ,  $\kappa_{CMG} = 24$  W  $\text{m}^{-1}$   $\text{K}^{-1}$ , and  $L = 6$  mm, the  $\Delta T_{CMG}$  comes out to be 32.5  $\mu\text{K}$ . Using this and  $V_{ANE}$ , the calculated value of  $S_{ANE}$  comes out to be 0.41  $\mu\text{V}/\text{K}$  for CMG (20 nm). Though high values of anomalous Nernst coefficients are reported in the literature for CMG thin films, here it is pointed out that the out-of-plane magnetized (OPM) configuration (the geometry in which the applied field is in the perpendicular direction and the temperature gradient is parallel to the film plane [see Fig. 6(b)]) is employed in all those experiments [3,73,74]. The large ANE observed is attributed to the large AHE in  $\text{Co}_2\text{MnGa}$ , both arising from a large net Berry curvature near the Fermi energy associated with nodal lines and Weyl points [29,71]. Consistent with these reports, we have also reported a large spin Hall angle, i.e., high transverse conductivity for the 20-nm CMG film in our previous report [24]. To the best of our knowledge, there is no literature available to compare the  $V_{ANE}$  values determined in the present case of polycrystalline  $\text{Co}_2\text{MnGa}$  films for the IPM configuration.

To confirm the presence of the LSSE in the case of CMG/NM bilayers, it is important to separate the spin current induced signal from the ANE. It can be done by comparing the transverse thermospin voltage in an IPM (the LSSE setup) and OPM configuration as shown in Figs. 6(a) and 6(b), respectively. In CMG/NM bilayers, the  $V_{th}$  consists of both  $V_{SSE}$  and  $V_{ANE}$  in the IPM configuration. Whereas, in the OPM configuration, only the ANE signal will appear as the temperature gradient, magnetization, and measured voltage direction are perpendicular to each other. The LSSE signal will not be present in this case as the spin current direction ( $\vec{J}_S$ ) is parallel

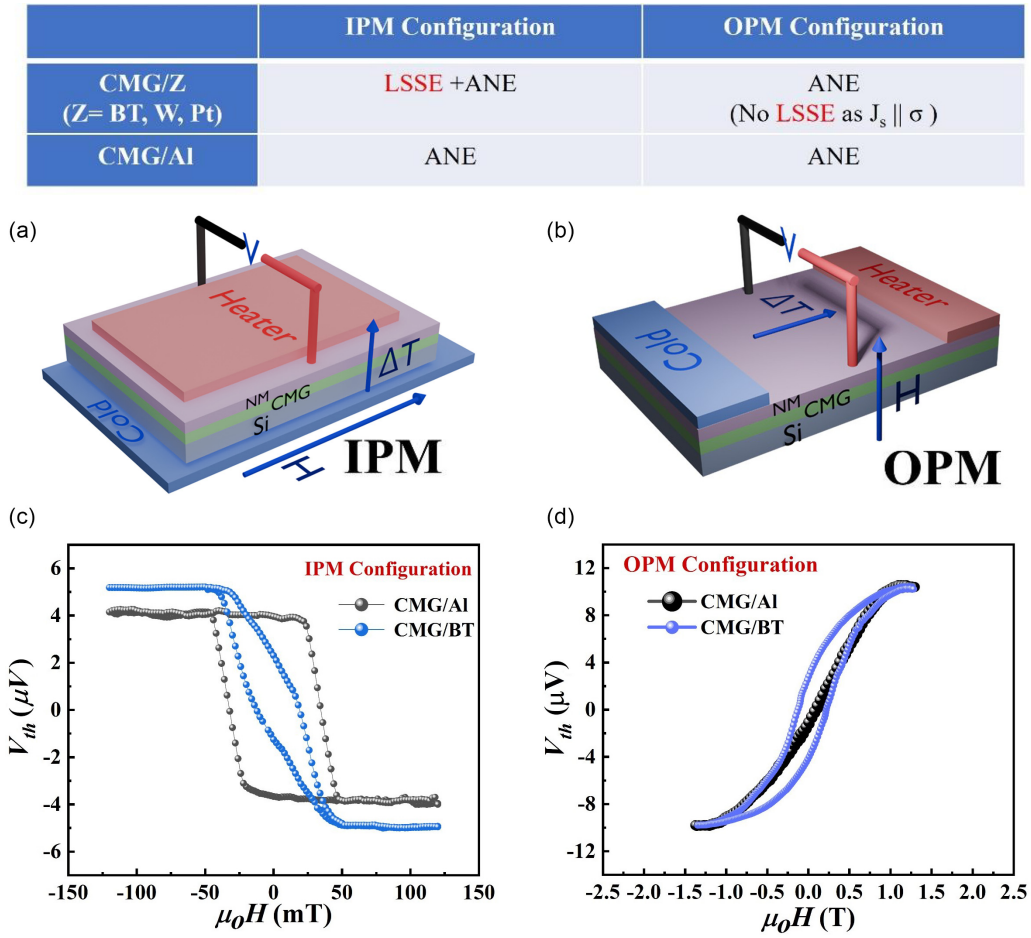


FIG. 6. (a) and (b) Schematics for the in-plane magnetized (IPM) and out-of-plane magnetized (OPM) configurations. (c) and (d) Thermospin voltage (spin Seebeck+anomalous Nernst voltage) (for CMG/BT) and anomalous Nernst voltage ( $V_{ANE}$ ) (for CMG/AI) vs applied magnetic field in IPM and OPM configurations, respectively.

to the spin polarization ( $\vec{\sigma}$ ) [ $\vec{E}_{ISHE} \propto (\vec{J}_s \times \vec{\sigma})$ ]. It should also be noted that in case of the OPM configuration, the resultant voltage signal ( $V_{th}$ ) will not be contaminated by the ANE voltage due to the very small temperature gradient perpendicular to the CMG film plane (if any) due to the parallel orientation of  $\Delta T$  and the magnetization direction [75]. Therefore, the quantitative comparison of the voltage between these two signals gives the estimation of the LSSE signal present along with the ANE in CMG/NM bilayer.

Figure 6(c) represents the magnetic field dependence of  $V_{th}$  (LSSE+ANE) for CMG/BT and  $V_{th} = V_{ANE}$  for CMG/AI in the IPM configuration. For the same samples, the measurement of the ANE voltage vs magnetic field is done in the OPM configuration as shown in Fig. 6(d). The Nernst coefficients measured on these two samples are quantitatively equal indicating the contribution of the ANE separated from the LSSE in CMG/BT bilayer. The anomalous Nernst coefficient  $S_{ANE}$  in the OPM is estimated as  $S_{ANE} = \frac{V_{ANE} L_x}{(L_y \Delta T_{CMG})}$ , where  $L_x$  is the length of the sample along which the temperature gradient is applied. The  $\Delta T$  is measured as 23 K at the two ends of the sample using temperature sensors. Considering  $V_{ANE} = 10.14 \mu\text{V}$ ,  $L_x = 5.5 \text{ mm}$ , and  $L_y = 4.5 \text{ mm}$ , the  $S_{ANE}$  is estimated as  $0.54 \pm 0.08 \mu\text{V/K}$ . From these results, it can

be concluded that for the polycrystalline CMG thin film, the anomalous Nernst coefficient is isotropic for different measurement configurations.

Now, the quantitative estimation of the spin Seebeck coefficient is done using the data measured in Fig. 5(a) in the IPM configuration (the LSSE setup). Considering the two contributions (SSE and ANE), the resultant voltage measured across the NM layer ( $V_{th}$ ) of the CMG/NM heterostructure can be written as

$$V_{th} = V_{SSE} + V_{ANE}^{supp}. \quad (10)$$

The suppressed ANE ( $V_{ANE}^{supp}$ ) voltage measured in CMG/NM bilayer can be calculated from the  $V_{ANE}$  data obtained on the isolated CMG layer and by considering the parallel circuit configuration of the CMG and NM layers, which is given by Eq. (11) [76–78],

$$V_{ANE}^{supp} = \left( \frac{r}{1+r} \right) V_{ANE}, \quad (11)$$

where  $V_{ANE}$  is the ANE voltage of a single metallic FM layer, and  $r = (\rho_{NM}/\rho_{CMG})(t_{CMG}/t_{NM})$ , with  $\rho_{NM}$  and  $\rho_{CMG}$  representing the resistivities of the NM and CMG layers and  $t_{NM}$

TABLE IV. Spin Seebeck voltage signal, thermal conductivity, temperature gradient across interface, and spin Seebeck coefficient for different systems under study.

	$V_{ANE}$ ( $\mu\text{V}$ )	Anomalous Nernst effect $\kappa$ ( $\text{W m}^{-1} \text{K}^{-1}$ )	$\Delta T_{CMG/NM}$ ( $\mu\text{K}$ )	$S_{ANE}$ ( $\mu\text{V/K}$ )
CMG(20)/Al(3)	3.98	24 (CMG)	32.53	$0.41 \pm 0.06$
	$V_{SSE}$ ( $\mu\text{V}$ )	Spin Seebeck effect $\kappa$ ( $\text{W m}^{-1} \text{K}^{-1}$ )	$\Delta T_{CMG/NM}$ (mK)	$S_{SSE}$ (nV/K)
CMG(20)/BT(10)	1.75	1.47 (BT)	11.20	$0.52 \pm 0.04$
CMG(20)/W(10)	-0.81	68 (W)	3.68	$0.73 \pm 0.03$
CMG(20)/Pt(10)	0.91	71 (Pt)	3.67	$0.83 \pm 0.04$

and  $t_{CMG}$  representing their thicknesses, respectively. It should be pointed out that different voltages appearing in Eqs. (10) and (11) correspond to the values in the magnetic saturated state.

Furthermore, the  $V_{SSE}$  is calculated [using Eq. (10)] from the background corrected values of  $V_{th}$  given by [76]

$$V_{th} = \left[ \frac{V_{th}(+\mu_0 H_{sat}) - V_{th}(-\mu_0 H_{sat})}{2} \right]. \quad (12)$$

Finally, the obtained values of  $V_{SSE}$  for CMG/BT, CMG/W, and CMG/Pt are 1.75, -0.81, and 0.91  $\mu\text{V}$ , respectively. To calculate the spin Seebeck coefficient  $S_{SSE}$ , the temperature gradient across the CMG/NM interfaces ( $\Delta T_{CMG/NM}$ ) is modeled using the COMSOL software and the obtained values are presented in Table IV. Using  $S_{SSE} = \frac{V_{SSE} t}{(L_y \Delta T_{CMG/NM})}$ , the estimated values of  $S_{SSE}$  is tabulated in Table IV.

The efficiency of spin-to-charge conversion in terms of the  $V_{SSE}$  voltage can now be qualitatively compared to  $V_{ISHE}$  considering the magnetic proximity effect remains the same in both the cases. It is evident that both the measurements (i.e., ISHE and SSE) performed on the CMG/NM heterostructures are in consonance with each other.

#### IV. CONCLUSION

In conclusion, we have studied the spin pumping and inverse spin Hall effect in  $\text{Co}_2\text{MnGa}/\text{NM}$  systems where  $\text{NM} = \text{Bi}_2\text{Te}_3$ , W, and Pt. We have found that spin pumping and effective spin mixing conductance were highest in  $\text{Co}_2\text{MnGa}/\text{W}$  ( $1.8 \pm 0.2 \times 10^{19} \text{ m}^{-2}$ ) and lowest in  $\text{Co}_2\text{MnGa}/\text{Pt}$  ( $0.8 \pm 0.1 \times 10^{19} \text{ m}^{-2}$ ). The parameters such as interface roughness, magnetic proximity effect, and spin backflow tendency critically contribute to determining the spin pumping and effective spin mixing conductance. The SHA value of  $\sim -0.08$  is reported for CMG/ $\alpha$ -W bilayer, which is remarkably high as compared to other reported values on the FM/ $\alpha$ -W system [35]. Despite  $\text{Co}_2\text{MnGa}/\text{Bi}_2\text{Te}_3$  having the lowest effective spin current density and higher resistivity, it exhibited the highest spin Hall angle ( $\sim 1.5$ ) among the bilayer systems under study (and the reported values for BT in literature [18]) due to its superior spin-orbit coupling strength. Therefore, the present results about the spin-to-charge conversion hold a great potential in favor of the  $\text{Co}_2\text{MnGa}/\text{Bi}_2\text{Te}_3$  system towards its use as an efficient spin charge converter based on FM/TI integration. The spin conversion efficiency of three heavy metals is confirmed by the thermospin measurements. The anomalous Nernst coefficient ( $S_{ANE}$ ) of 0.41  $\mu\text{V/K}$  for the 20-nm CMG thin film is obtained in the in-plane magnetized geometry. The spin Seebeck voltage measurements on these heterostructures are in excellent agreement with the findings from the ISHE measurements.

- [1] P. Hosur and X. Qi, Recent developments in transport phenomena in Weyl semimetals, *C. R. Phys.* **14**, 857 (2013).
- [2] S. S. L. Zhang, A. A. Burkov, I. Martin, and O. G. Heinonen, Spin-to-charge conversion in magnetic Weyl semimetals, *Phys. Rev. Lett.* **123**, 187201 (2019).
- [3] H. Reichlova, R. Schlitz, S. Beckert, P. Swekis, A. Markou, Y. C. Chen, S. Fabretti, G. H. Park, A. Niemann, S. Sudheendra *et al.*, Large anomalous Nernst effect in thin films of the Weyl semimetal  $\text{Co}_2\text{MnGa}$ , *Appl. Phys. Lett.* **113**, 21 (2018).
- [4] Y. Zhang, Y. Yin, G. Dubuis, T. Butler, N. V. Medhekar, and S. Granville, Berry curvature origin of the thickness-dependent anomalous Hall effect in a ferromagnetic Weyl semimetal, *npj Quantum Mater.* **6**, 1 (2021).
- [5] P. Swekis, A. S. Sukhanov, Y. C. Chen, A. Gloskovskii, G. H. Fecher, I. Panagiotopoulos, J. Sichelschmidt, V. Ukleev, A.

Devshvili, A. Vorobiev *et al.*, Magnetic and electronic properties of Weyl semimetal  $\text{Co}_2\text{MnGa}$  thin films, *Nanomaterials* **11**, 1 (2021).

- [6] S. Hait, N. K. Gupta, N. Sharma, L. Pandey, N. Kumar, V. Barwal, P. Kumar, and S. Chaudhary, Spin pumping in nanolayers of  $\text{WS}_2/\text{Co}_2\text{FeAl}$  heterostructures: Large spin mixing conductance and spin transparency, *J. Appl. Phys.* **132**, 13 (2022).
- [7] W. Zhang, W. Han, X. Jiang, S. H. Yang, and S. S. P. Parkin, Role of transparency of platinum-ferromagnet interfaces in determining the intrinsic magnitude of the spin Hall effect, *Nat. Phys.* **11**, 496 (2015).
- [8] E. Saitoh, M. Ueda, H. Miyajima, and G. Tatara, Conversion of spin current into charge current at room temperature: Inverse spin-Hall effect, *Appl. Phys. Lett.* **88**, 18 (2006).

- [9] K. Uchida, S. Takahashi, K. Harii, J. Ieda, W. Koshibae, K. Ando, S. Maekawa, and E. Saitoh, Observation of the spin Seebeck effect, *Nature (London)* **455**, 778 (2008).
- [10] T. Jungwirth, J. Wunderlich, and K. Olejník, Spin Hall effect devices, *Nat. Mater.* **11**, 382 (2012).
- [11] A. Hoffmann, Spin Hall effects in metals, *IEEE Trans. Magn.* **49**, 5172 (2013).
- [12] K. Uchida, M. Ishida, T. Kikkawa, A. Kirihara, T. Murakami, and E. Saitoh, Erratum: Longitudinal spin Seebeck effect: From fundamentals to applications, *J. Phys.: Condens. Matter* **26**, 343202 (2014).
- [13] J. Holanda, O. Alves Santos, R. O. Cunha, J. B. S. Mendes, R. L. Rodríguez-Suárez, A. Azevedo, and S. M. Rezende, Longitudinal spin Seebeck effect in permalloy separated from the anomalous Nernst effect: Theory and experiment, *Phys. Rev. B* **95**, 214421 (2017).
- [14] Y. Tserkovnyak, A. Brataas, G. E. W. Bauer, and B. I. Halperin, Nonlocal magnetization dynamics in ferromagnetic heterostructures, *Rev. Mod. Phys.* **77**, 1375 (2005).
- [15] Y. Tserkovnyak, A. Brataas, and G. E. W. Bauer, Enhanced Gilbert damping in thin ferromagnetic films, *Phys. Rev. Lett.* **88**, 117601 (2002).
- [16] V. E. Demidov, S. Urazhdin, G. de Loubens, O. Klein, V. Cros, A. Anane, and S. O. Demokritov, Magnetization oscillations and waves driven by pure spin currents, *Phys. Rep.* **673**, 1 (2017).
- [17] H. H. Huy, N. H. D. Khang, J. Sasaki, S. Namba, P. N. Hai, Q. Le, B. York, C. Hwang, X. Liu, M. Gribelyuk *et al.*, Large inverse spin Hall effect in BiSb topological insulator for 4 Tb/In<sup>2</sup> magnetic recording technology, *Appl. Phys. Lett.* **122**, 5 (2023).
- [18] K. Kondou, R. Yoshimi, A. Tsukazaki, Y. Fukuma, J. Matsuno, K. S. Takahashi, M. Kawasaki, Y. Tokura, and Y. Otani, Fermi-level-dependent charge-to-spin current conversion by Dirac surface states of topological insulators, *Nat. Phys.* **12**, 1027 (2016).
- [19] E. Longo, M. Belli, M. Alia, M. Rimoldi, R. Cecchini, M. Longo, C. Wiemer, L. Locatelli, P. Tsipas, A. Dimoulas *et al.*, Large spin-to-charge conversion at room temperature in extended epitaxial Sb<sub>2</sub>Te<sub>3</sub> topological insulator chemically grown on silicon, *Adv. Funct. Mater.* **32**, 4 (2022).
- [20] Y. Fan, P. Upadhyaya, X. Kou, M. Lang, S. Takei, Z. Wang, J. Tang, L. He, L. T. Chang, M. Montazeri *et al.*, Magnetization switching through giant spin-orbit torque in a magnetically doped topological insulator heterostructure, *Nat. Mater.* **13**, 699 (2014).
- [21] J. C. Tung and G. Y. Guo, High spin polarization of the anomalous Hall current in Co-based Heusler compounds, *New J. Phys.* **15**, 033014 (2013).
- [22] Y. Sun, Y. Zhang, C. Felser, and B. Yan, Strong intrinsic spin Hall effect in the TaAs family of Weyl semimetals, *Phys. Rev. Lett.* **117**, 146403 (2016).
- [23] L. Leiva, S. Granville, Y. Zhang, S. Dushenko, E. Shigematsu, T. Shinjo, R. Ohshima, Y. Ando, and M. Shiraishi, Giant spin Hall angle in the Heusler alloy Weyl ferromagnet Co<sub>2</sub>MnGa, *Phys. Rev. B* **103**, L041114 (2021).
- [24] N. Sharma, L. Pandey, N. Kumar, N. K. Gupta, S. Hait, V. Mishra, A. Kumar, and S. Chaudhary, Magnetic and anomalous Hall effect investigations of co-sputtered Co<sub>2</sub>MnGa Heusler alloy thin films, *J. Appl. Phys.* **134**, 17 (2023).
- [25] C. Guillemard, S. Petit-Watelot, L. Pasquier, D. Pierre, J. Ghanbaja, J.-C. Rojas-Sánchez, A. Bataille, J. Rault, P. Le Fèvre, F. Bertran *et al.*, Ultralow magnetic damping in Co<sub>2</sub>Mn-based Heusler compounds: Promising materials for spintronics, *Phys. Rev. Appl.* **11**, 064009 (2019).
- [26] H. Chudo, K. Ando, K. Saito, S. Okayasu, R. Haruki, Y. Sakuraba, H. Yasuoka, K. Takanashi, and E. Saitoh, Spin pumping efficiency from half metallic Co<sub>2</sub>MnSi, *J. Appl. Phys.* **109**, 7 (2011).
- [27] S. Bosu, Y. Sakuraba, K. Uchida, K. Saito, T. Ota, E. Saitoh, and K. Takanashi, Spin Seebeck effect in thin films of the Heusler compound Co<sub>2</sub>MnSi, *Phys. Rev. B* **83**, 224401 (2011).
- [28] M. V. Lopes, E. C. de Souza, J. G. Santos, J. M. de Araujo, L. Lima, A. B. de Oliveira, F. Bohn, and M. A. Correa, Modulating the spin Seebeck effect in Co<sub>2</sub>FeAl Heusler alloy for sensor applications, *Sensors (Switzerland)* **20**, 5 (2020).
- [29] J. Hu, S. Granville, and H. Yu, Spin-dependent thermoelectric transport in cobalt-based Heusler alloys, *Ann. Phys.* **532**, 11 (2020).
- [30] L. Pandey, S. Husain, X. Chen, V. Barwal, S. Hait, N. K. Gupta, V. Mishra, A. Kumar, N. Sharma, N. Kumar *et al.*, Weak antilocalization and electron-electron interactions in topological insulator Bi<sub>x</sub>Te<sub>y</sub> films deposited by sputtering on Si(100), *Phys. Rev. Mater.* **6**, 044203 (2022).
- [31] See Supplemental Material at <http://link.aps.org/supplemental/10.1103/PhysRevB.110.094402> for details of the deposition parameter, details of the instrumentation and measurement parameters, investigation of the topological properties of Bi<sub>2</sub>Te<sub>3</sub> films, XRR profiles, MOKE data, the out-of-plane MH loops of the CMG/Al and three CMG/NM bilayer system, modeling of the temperature gradient at different interfaces in CMG/NM bilayers, effective damping ( $\alpha_{\text{eff}}$ ) values at different thicknesses of NM layers for bilayer systems under study, and the FMR response and SIMS measurement on Si//CMG/BT and Si//BT/CMG heterostructures, which includes Refs. [24,79–84].
- [32] T. S. Safi, C. T. Chou, J. T. Hou, J. Han, and L. Liu, Spin-generation in magnetic Weyl semimetal Co<sub>2</sub>MnGa across varying degree of chemical order, *Appl. Phys. Lett.* **121**, 9 (2022).
- [33] A. Kumar, N. Pandey, D. Kumar, M. Gupta, S. Chaudhary, and P. K. Muduli, Influence of annealing on spin pumping in sputtered deposited Co/Pt bilayer thin films, *Phys. B (Amsterdam, Neth.)* **570**, 254 (2019).
- [34] H. L. Wang, C. H. Du, Y. Pu, R. Adur, P. C. Hammel, and F. Y. Yang, Large spin pumping from epitaxial Y<sub>3</sub>Fe<sub>5</sub>O<sub>12</sub> thin films to Pt and W layers, *Phys. Rev. B* **88**, 100406(R) (2013).
- [35] C. F. Pai, L. Liu, Y. Li, H. W. Tseng, D. C. Ralph, and R. A. Buhrman, Spin transfer torque devices utilizing the giant spin Hall effect of tungsten, *Appl. Phys. Lett.* **101**, 12 (2012).
- [36] W. B. Liao, T. Y. Chen, Y. Ferrante, S. S. P. Parkin, and C. F. Pai, Current-induced magnetization switching by the high spin Hall conductivity  $\alpha$ -W, *Phys. Status Solidi RRL* **13**, 11 (2019).
- [37] M. Obstbaum, M. Decker, A. K. Greitner, M. Haertinger, T. N. G. Meier, M. Kronseder, K. Chadova, S. Wimmer, D. Ködderitzsch, H. Ebert *et al.*, Tuning spin Hall angles by alloying, *Phys. Rev. Lett.* **117**, 167204 (2016).
- [38] L. Pandey, S. Husain, V. Barwal, S. Hait, N. K. Gupta, V. Mishra, N. Kuma, D. Dixit, N. Sharma, V. Singh *et al.*, Topological transport properties of highly oriented Bi<sub>2</sub>Te<sub>3</sub> thin film

- deposited by sputtering, *J. Phys.: Condens. Matter* **35**, 355702 (2023).
- [39] S. Hait, S. Husain, V. Barwal, L. Pandey, N. Sharma, N. K. Gupta, N. Kumar, and S. Chaudhary, High spin mixing conductance and spin transparency in ion-beam sputtered Ta/Co<sub>60</sub>Fe<sub>20</sub>B<sub>20</sub> bilayers on Si(100), *Surf. Interfaces* **33**, 102259 (2022).
- [40] S. Hait, S. Husain, V. Barwal, N. K. Gupta, L. Pandey, P. Svedlindh, and S. Chaudhary, Comparison of high temperature growth versus post-deposition in situ annealing in attaining very low Gilbert damping in sputtered Co<sub>2</sub>FeAl Heusler alloy films, *J. Magn. Magn. Mater.* **519**, 167509 (2021).
- [41] S. Azzawi, A. T. Hindmarch, and D. Atkinson, Magnetic damping phenomena in ferromagnetic thin-films and multilayers, *J. Phys. D: Appl. Phys.* **50**, 473001 (2017).
- [42] C. Kittel, On the theory of ferromagnetic resonance absorption, *Phys. Rev.* **73**, 155 (1948).
- [43] J. C. Rojas-Sánchez, N. Reyren, P. Laczkowski, W. Savero, J. P. Attané, C. Deranlot, M. Jamet, J. M. George, L. Vila, and H. Jaffrès, Spin pumping and inverse spin Hall effect in platinum: The essential role of spin-memory loss at metallic interfaces, *Phys. Rev. Lett.* **112**, 106602 (2014).
- [44] L. Zhu, L. Zhu, and R. A. Buhrman, Fully spin-transparent magnetic interfaces enabled by the insertion of a thin paramagnetic NiO layer, *Phys. Rev. Lett.* **126**, 107204 (2021).
- [45] K. Hasegawa, Y. Hibino, M. Suzuki, T. Koyama, and D. Chiba, Enhancement of spin-orbit torque by inserting CoO<sub>x</sub> layer into Co/Pt interface, *Phys. Rev. B* **98**, 020405(R) (2018).
- [46] M. Jamali, J. S. Lee, J. S. Jeong, F. Mahfouzi, Y. Lv, Z. Zhao, B. K. Nikolić, K. A. Mkhoyan, N. Samarth, and J. P. Wang, Giant spin pumping and inverse spin Hall effect in the presence of surface and bulk spin-orbit coupling of topological insulator Bi<sub>2</sub>Se<sub>3</sub>, *Nano Lett.* **15**, 7126 (2015).
- [47] V. M. Pereira, S. G. Altendorf, C. E. Liu, S. C. Liao, A. C. Komarek, M. Guo, H.-J. Lin, C. T. Chen, M. Hong, J. Kwo *et al.*, Topological insulator interfaced with ferromagnetic insulators: Bi<sub>2</sub>Te<sub>3</sub> thin films on magnetite and iron garnets, *Phys. Rev. Mater.* **4**, 064202 (2020).
- [48] S. Hait, S. Husain, H. Bangar, L. Pandey, V. Barwal, N. Kumar, N. K. Gupta, V. Mishra, N. Sharma, P. Gupta *et al.*, Spin pumping through different spin-orbit coupling interfaces in  $\beta$ -W/interlayer/Co<sub>2</sub>FeAl heterostructures, *ACS Appl. Mater. Interfaces* **14**, 37182 (2022).
- [49] J. M. Shaw, H. T. Nembach, and T. J. Silva, Determination of spin pumping as a source of linewidth in sputtered Co<sub>90</sub>Fe<sub>10</sub>/Pd multilayers by use of broadband ferromagnet, *Phys. Rev. B* **85**, 054412 (2012).
- [50] S. Hait, S. Husain, N. K. Gupta, N. Behera, A. Kumar, R. Gupta, V. Barwal, L. Pandey, P. Svedlindh, and S. Chaudhary, Impact of ferromagnetic layer thickness on the spin pumping in Co<sub>60</sub>Fe<sub>20</sub>B<sub>20</sub>/Ta bilayer thin films, *J. Mater. Sci. Mater. Electron.* **32**, 12453 (2021).
- [51] M. H. Nguyen, D. C. Ralph, and R. A. Buhrman, Spin torque study of the spin Hall conductivity and spin diffusion length in platinum thin films with varying resistivity, *Phys. Rev. Lett.* **116**, 126601 (2016).
- [52] Q. Hao, W. Chen, and G. Xiao, Beta ( $\beta$ ) tungsten thin films: Structure, electron transport, and giant spin Hall effect, *Appl. Phys. Lett.* **106**, 18 (2015).
- [53] E. Sagasta, Y. Omori, M. Isasa, M. Gradhand, L. E. Hueso, Y. Niimi, Y. Otani, and F. Casanova, Tuning the spin Hall effect of Pt from the moderately dirty to the superclean regime, *Phys. Rev. B* **94**, 060412 (2016).
- [54] D. Hahjria, N. Behera, D. K. Pandya, and S. Chaudhary, Dependence of spin pumping in W/CoFeB heterostructures on the structural phase of tungsten, *Phys. Rev. B* **99**, 014430 (2019).
- [55] F. B. Abdulahad, J. H. Lin, Y. Liou, W. K. Chiu, L. J. Chang, M. Y. Kao, J. Z. Liang, D. S. Hung, and S. F. Lee, Spin chemical potential bias induced surface current evidenced by spin pumping into the topological insulator Bi<sub>2</sub>Te<sub>3</sub>, *Phys. Rev. B* **92**, 241304(R) (2015).
- [56] Y. Tserkovnyak, A. Brataas, and G. E. W. Bauer, Spin pumping and magnetization dynamics in metallic multilayers, *Phys. Rev. B* **66**, 224403 (2002).
- [57] W. Cao, J. Liu, A. Zangiabadi, K. Barmak, and W. E. Bailey, Measurement of spin mixing conductance in Ni<sub>81</sub>Fe<sub>19</sub>/ $\alpha$ -W and Ni<sub>81</sub>Fe<sub>19</sub>/ $\beta$ -W heterostructures via ferromagnetic resonance, *J. Appl. Phys.* **126**, 4 (2019).
- [58] Q. Lu, Y. Li, B. Peng, H. Tang, Y. Zhang, Z. He, L. Wang, C. Li, W. Su, Q. Yang *et al.*, Enhancement of the spin-mixing conductance in Co-Fe-B/W bilayers by interface engineering, *Phys. Rev. Appl.* **12**, 064035 (2019).
- [59] K. Sriram, R. Mondal, J. Pradhan, A. Haldar, and C. Murapaka, Structural phase engineering of ( $\alpha + \beta$ )-W for a large spin Hall angle and spin diffusion length, *J. Phys. Chem. C* **127**, 22704 (2023).
- [60] B. B. Singh, K. Roy, P. Gupta, T. Seki, K. Takashi, and S. Bedanta, High spin mixing conductance and spin interface transparency at the interface of a Co<sub>2</sub>Fe<sub>0.4</sub>Mn<sub>0.6</sub>Si Heusler alloy and Pt, *NPG Asia Mater.* **13**, 1 (2021).
- [61] S. M. Farzaneh and S. Rakheja, Intrinsic spin Hall effect in topological insulators: A first-principles study, *Phys. Rev. Mater.* **4**, 114202 (2020).
- [62] H. Wu, P. Zhang, P. Deng, Q. Lan, Q. Pan, S. A. Razavi, X. Che, L. Huang, B. Dai, K. Wong *et al.*, Room-temperature spin-orbit torque from topological surface states, *Phys. Rev. Lett.* **123**, 207205 (2019).
- [63] M. Dc, J. Y. Chen, T. Peterson, P. Sahu, B. Ma, N. Mousavi, R. Harjani, and J. P. Wang, Observation of high spin-to-charge conversion by sputtered bismuth selenide thin films at room temperature, *Nano Lett.* **19**, 4836 (2019).
- [64] M. Dc, R. Grassi, J. Y. Chen, M. Jamali, D. Reifsnnyder Hickey, D. Zhang, Z. Zhao, H. Li, P. Quarterman, Y. Lv *et al.*, Room-temperature high spin-orbit torque due to quantum confinement in sputtered Bi<sub>x</sub>Se<sub>(1-x)</sub> films, *Nat. Mater.* **17**, 800 (2018).
- [65] A. R. Mellnik, J. S. Lee, A. Richardella, J. L. Grab, P. J. Mintun, M. H. Fischer, A. Vaezi, A. Manchon, E.-A. Kim, N. Samarth *et al.*, Spin-transfer torque generated by a topological insulator, *Nature (London)* **511**, 449 (2014).
- [66] W. Skowroński, Ł. Karwacki, S. Ziętek, J. Kanak, S. Łazarski, K. Grochot, T. Stobiecki, P. Kuświk, F. Stobiecki, and J. Barnaś, Determination of spin Hall angle in heavy metal/CoFeB-based heterostructures with interfacial spin-orbit fields, *Phys. Rev. Appl.* **11**, 024039 (2019).
- [67] L. Qian, K. Wang, Y. Zheng, and G. Xiao, Spin Hall effect in the  $\alpha$  and  $\beta$  phases of Ta<sub>x</sub>W<sub>1-x</sub> alloys, *Phys. Rev. B* **102**, 094438 (2020).

- [68] M. Harder, Y. Gui, and C.-M. Hu, Electrical detection of magnetization dynamics via spin rectification effects, *Phys. Rep.* **661**, 1 (2016).
- [69] R. Iguchi and E. Saitoh, Measurement of spin pumping voltage separated from extrinsic microwave effects, *J. Phys. Soc. Jpn.* **86**, 1 (2017).
- [70] H. Adachi, K. I. Uchida, E. Saitoh, and S. Maekawa, Theory of the spin Seebeck effect, *Rep. Prog. Phys.* **76**, 21 (2013).
- [71] A. Sakai, Y. P. Mizuta, A. A. Nugroho, R. Sihombing, T. Koretsune, M. T. Suzuki, N. Takemori, R. Ishii, D. Nishio-Hamane, R. Arita *et al.*, Giant anomalous Nernst effect and quantum-critical scaling in a ferromagnetic semimetal, *Nat. Phys.* **14**, 1119 (2018).
- [72] M. Gamino, J. G. S. Santos, A. L. R. Souza, A. S. Melo, R. D. Della Pace, E. F. Silva, A. B. Oliveira, R. L. Rodríguez-Suárez, F. Bohn, and M. A. Correa, Longitudinal spin Seebeck effect and anomalous Nernst effect in CoFeB/non-magnetic metal bilayers, *J. Magn. Magn. Mater.* **527**, 167778 (2021).
- [73] J. Hu, Y. Zhang, M. A. Z. Cabero, B. Wei, S. Tu, S. Liu, D. Yu, J. P. Ansermet, S. Granville, and H. Yu, Anomalous Nernst effect in Co<sub>2</sub>MnGa thin films with perpendicular magnetic anisotropy, *J. Magn. Magn. Mater.* **500**, 3 (2020).
- [74] S. N. Guin, K. Manna, J. Noky, S. J. Watzman, C. Fu, N. Kumar, W. Schnelle, C. Shekhar, Y. Sun, J. Gooth *et al.*, Anomalous Nernst effect beyond the magnetization scaling relation in the ferromagnetic Heusler compound Co<sub>2</sub>MnGa, *NPG Asia Mater.* **11**, 1 (2019).
- [75] T. Kikkawa, K. Uchida, S. Daimon, Y. Shiomi, H. Adachi, Z. Qiu, D. Hou, X. F. Jin, S. Maekawa, and E. Saitoh, Separation of longitudinal spin Seebeck effect from anomalous Nernst effect: Determination of origin of transverse thermoelectric voltage in metal/insulator junctions, *Phys. Rev. B* **88**, 214403 (2013).
- [76] A. Chanda, D. Rani, D. DeTellem, N. Alzahrani, D. A. Arena, S. Witanachchi, R. Chatterjee, M. H. Phan, and H. Srikanth, Large thermo-spin effects in Heusler alloy-based spin gapless semiconductor thin films, *ACS Appl. Mater. Interfaces* **15**, 53697 (2023).
- [77] P. Bougiatioti, C. Klewe, D. Meier, O. Manos, O. Kuschel, J. Wollschläger, L. Bouchenoire, S. D. Brown, J. M. Schmalhorst, G. Reiss *et al.*, Quantitative disentanglement of the spin Seebeck, proximity-induced, and ferromagnetic-induced anomalous Nernst effect in normal-metal-ferromagnet bilayers, *Phys. Rev. Lett.* **119**, 227205 (2017).
- [78] R. Ramos, T. Kikkawa, K. Uchida, H. Adachi, I. Lucas, M. H. Aguirre, P. Algarabel, L. Morellon, S. Maekawa, E. Saitoh *et al.*, Observation of the spin Seebeck effect in epitaxial Fe<sub>3</sub>O<sub>4</sub> thin films, *Appl. Phys. Lett.* **102**, 7 (2013).
- [79] H.-Z. Lu and S.-Q. Shen, Weak localization and weak anti-localization in topological insulators, *SPIE Proc.* **9167**, 263 (2014).
- [80] M. Lang, L. He, X. Kou, P. Upadhyaya, Y. Fan, H. Chu, Y. Jiang, J. H. Bardarson, W. Jiang, E. S. Choi *et al.*, Competing weak localization and weak antilocalization in ultrathin topological insulators, *Nano Lett.* **13**, 48 (2013).
- [81] L. Bao, L. He, N. Meyer, X. Kou, P. Zhang, Z. G. Chen, A. V. Fedorov, J. Zou, T. M. Riedemann, T. A. Lograsso *et al.*, Weak anti-localization and quantum oscillations of surface states in topological insulator Bi<sub>2</sub>Se<sub>2</sub>Te, *Sci. Rep.* **2**, 726 (2012).
- [82] A. Roy, S. Guchhait, S. Sonde, R. Dey, T. Pramanik, A. Rai, H. C. P. Movva, L. Colombo, and S. K. Banerjee, Two-dimensional weak anti-localization in Bi<sub>2</sub>Te<sub>3</sub> thin film grown on Si(111)-(7 × 7) surface by molecular beam epitaxy, *Appl. Phys. Lett.* **102**, 16 (2013).
- [83] J. Wang, A. M. Dasilva, C. Z. Chang, K. He, J. K. Jain, N. Samarth, X. C. Ma, Q. K. Xue, and M. H. W. Chan, Evidence for electron-electron interaction in topological insulator thin films, *Phys. Rev. B* **83**, 245438 (2011).
- [84] B. M. Ludbrook, B. J. Ruck, and S. Granville, Perpendicular magnetic anisotropy in Co<sub>2</sub>MnGa and its anomalous Hall effect, *Appl. Phys. Lett.* **110**, 6 (2017).